

The double-diffusive modon

TIMOUR RADKO

Department of Oceanography, Naval Postgraduate School, Monterey, CA 93943, USA
tradko@nps.edu

(Received 26 March 2007 and in revised form 11 April 2008)

Fully developed two-dimensional salt-finger convection is characterized by the appearance of coherent dipolar eddies which carry relatively fresh and cold fluid upward and salty and warm fluid downward. Such structures – the double-diffusive modons – are prevalent in the regime in which density stratification is close to neutral and the salt-finger instability is extremely vigorous. The structure and translation velocities of modons are discussed in terms of the asymptotic expansion in which the background density ratio approaches unity. It is argued that the vertical salt flux is driven primarily by double-diffusive modons, which makes it possible to derive explicit expressions for the mixing rates of temperature and salinity as a function of their background gradients. Predictions of the proposed mixing model are successfully tested by direct numerical simulations.

1. Introduction

Geophysical fluid dynamics has never suffered from the lack of fascinating physical ideas and sleek mathematical solutions. However, even in the glamorous field of the twentieth century earth sciences some theories stand out as particularly elegant and insightful. Two of my personal favourites are the theory of double-diffusion (Stern 1960) and the model of isolated dipolar eddies known as ‘modons’ (Stern 1975*a*).

Double-diffusion is the instability of a stratified fluid at rest whose density is determined by two components diffusing at different rates. Stern (1960) demonstrated that such a configuration can be unstable even if the density of the fluid is increasing downwards. The resulting double-diffusive convection has long been recognized as a significant, and in many cases dominant, mixing process in the ocean. In the subtropical oceans, hot salty water is often located above the cold and fresh. Thus, the faster diffuser (temperature T) is stabilizing and the slower diffuser (salinity S) is destabilizing, leading to the salt-fingering form of double-diffusive convection. The modon solution was introduced (Stern 1975*a*; Larichev & Reznik 1976) to describe a closely packed vortex pair travelling together as a single entity – the oceanographically relevant extension of the Lamb dipole (Lamb 1895). While originally developed to explain the oceanographic phenomena, both double-diffusion and modon theories proved to be relevant for many other physical systems. Double-diffusion finds applications in chemistry, geology, and metallurgy, whereas the modon is a convenient prototype of structures commonly observed in meteorology, astrophysics, and plasma physics. In this paper we argue that the modon-type structures also emerge in the fully developed double-diffusive instability, and can play a key role in the vertical mixing of heat and salt.

To be specific, our discussion is focused on the salt-finger regime of double-diffusion; basic vertical gradients of temperature and salinity (\bar{T}_z, \bar{S}_z) are positive. The condition

for salt fingering (Stern 1960) is

$$1 < R_\rho < 1/\tau,$$

where $R_\rho = \alpha \bar{T}_z / (\beta \bar{S}_z)$ is the density ratio, (α, β) are the expansion/contraction coefficients of heat and salt, and $\tau = k_S / k_T$ is the diffusivity ratio of salt and heat. Numerical simulations (Shen & Veronis 1997; Merryfield & Grindler 1999; Stern, Radko & Simeonov 2001, Stern & Simeonov 2005) indicate that fingering convection can take very different forms, depending on the governing parameters. If $R_\rho \rightarrow 1/\tau$, the system is close to a point of marginal instability and salt fingers appear in the form of narrow vertically oriented filaments. The flow is largely laminar and the vertical temperature and salinity fluxes are weak. The magnitude and dynamics of salt fingers in this limit can be explained (Radko & Stern 1999, 2000) using conventional techniques of weakly nonlinear instability theory. Applicability of these methods, however, becomes questionable when R_ρ is far from the point of marginal instability, the situation which is generally realized in the oceanic double-diffusion ($1 < R_\rho < 3$ and $1/\tau \sim 100$). While promising attempts have been made (Balmforth *et al.* 2006) to formulate explicit models using the upper bound theory, accurate analytical description of double-diffusive convection for low values of R_ρ is still lacking.

The focus of our study is on the limit when R_ρ is close to unity and the background density is nearly uniform. The pattern of salt fingers in this regime changes dramatically. For $R_\rho \rightarrow 1^+$, the flow becomes highly turbulent and the vertical temperature and salinity fluxes greatly increase. The primary fastest growing instability is represented by the regular, exponentially amplifying structure – the elevator mode – regardless of R_ρ . However, such columnar structures cannot survive because of the secondary super-exponential instabilities, which become particularly active at low density ratios (Stern & Simeonov 2005). Long vertical salt fingers break into isolated round blobs. Sinking blobs carry warm and salty fluid downward whereas rising blobs are relatively cool and fresh. The resulting exchange of fluid provides an efficient mechanism for the vertical transport of heat and salt. Numerical solutions in this paper reveal that blobs consist of a roughly symmetric vortex pair; they propagate significant distances while preserving their shape and contain a region of trapped fluid. All these features are familiar to oceanographers – they fit perfectly the classical description of a modon. Of course, modons are usually discussed in the context of mesoscale (~ 100 km) dynamics, where they represent the horizontal pattern of circulation in isolated dipolar eddies. However, as we show here, they can also serve as an adequate conceptual model for the vertical structure of fully developed two-dimensional (x, z) salt fingers on scales of centimetres. Thus, the propagating dipolar structures in fully developed salt-finger flow will be hereafter referred to as double-diffusive modons.

Our study attempts to describe the structure and dynamics of double-diffusive modons analytically, by focusing on the asymptotic limit $R_\rho \rightarrow 1^+$. The proposed similarity solution is characterized by the streamfunction field which is dominated by the unit azimuthal wavenumber ($m = 1$) component. The theoretical significance of double-diffusive modons is related to their preferred propagation velocity and size, which are uniquely determined by the background density ratio. We assume and subsequently verify that the salt-finger field can be adequately represented by an array of rising and sinking double-diffusive modons – the microscale counterpart of Stern's (1975a) 'modon-sea' model. This assumption makes it possible to formulate a simple phenomenological model of equilibrium salt-finger convection which offers

explicit expressions for the key mixing characteristics, such as the vertical heat/salt fluxes and the kinetic energy dissipation rate.

Before discussing the vertical mixing driven by double-diffusive modons, it should be emphasized that our model describes only the local fluxes and their dependence on local T - S gradients; we are concerned here with spatial scales comparable to (or less than) the characteristic salt-finger width. As argued in Stern *et al.* (2001), these are the ‘small domain’ flux–gradient laws and inclusion of much greater scales in the model may reveal their secondary instabilities. The large-scale instabilities, in turn, can modify the uniform background stratification (Radko 2003, 2005), spontaneously generating stepped structures known as thermohaline staircases. These effects, however, are beyond the scope of this paper; our primary goal is to formulate a physically based *local* parameterization of fluxes for $R_\rho \rightarrow 1^+$.

This paper is set out as follows. In §2 we perform a set of preliminary two-dimensional numerical experiments, focusing our inquiry on structure and dynamics of the coherent dipolar eddies – the double-diffusive modons – in the limit $R_\rho \rightarrow 1^+$. The major characteristics of the simulated modons are rationalized by a formal asymptotic theory of §3 in which $\varepsilon = \sqrt{1 - R_\rho^{-1}}$ is small. The proposed model for the translation speed and T - S anomalies of double-diffusive modons provide a physically based means to calculate the magnitude and dependences of the vertical mixing rates of heat and salt (§4). In §4 we also revisit the direct numerical simulations to systematically test the mixing theory for small finite values of ε . We summarize and conclude in §5.

2. Preliminary considerations

2.1. Numerical simulations

Following Radko & Stern (1999), we separate the temperature and salinity fields into the basic state (\bar{T}, \bar{S}) , representing a uniform vertical gradient, and a departure (T, S) from it. The two-dimensional Boussinesq equations of motion are expressed in terms of T and S as

$$\left. \begin{aligned} \frac{\partial}{\partial t} \nabla^2 \psi + J(\psi, \nabla^2 \psi) &= g \frac{\partial}{\partial x} (\alpha T - \beta S) + \nu \nabla^4 \psi, \\ \frac{\partial T}{\partial t} + J(\psi, T) + \frac{\partial \psi}{\partial x} \frac{\partial \bar{T}}{\partial z} &= k_T \nabla^2 T, \\ \frac{\partial S}{\partial t} + J(\psi, S) + \frac{\partial \psi}{\partial x} \frac{\partial \bar{S}}{\partial z} &= k_S \nabla^2 S, \end{aligned} \right\} \quad (1)$$

where ν is the molecular viscosity, k_T, k_S are the diffusivities of heat and salt, ψ is the streamfunction, (α, β) are the expansion/contraction coefficients of the linear equation of state, and

$$J(a, b) = \frac{\partial a}{\partial x} \frac{\partial b}{\partial z} - \frac{\partial a}{\partial z} \frac{\partial b}{\partial x}$$

is the Jacobian.

We assume periodic boundary conditions for T, S and ψ in x and z and examine the resulting solutions. The system (1) is characterized by a set of integral invariants. Multiplying the temperature, salinity and vorticity equations in (1) by T, S and ψ respectively, and integrating the resulting equations over the doubly-periodic domain

and in time (e.g. Stern 1975*b*), we arrive at

$$\langle wT \rangle \frac{\partial \bar{T}}{\partial z} = k_T \langle |\nabla T|^2 \rangle, \quad (2a)$$

$$\langle wS \rangle \frac{\partial \bar{S}}{\partial z} = k_S \langle |\nabla S|^2 \rangle, \quad (2b)$$

$$g \langle w\beta S \rangle - g \langle w\alpha T \rangle = \nu \langle |\nabla \psi|^2 \rangle, \quad (2c)$$

where $\langle \dots \rangle$ denotes the space and time average; $(u, w) = (-\partial\psi/\partial z, \partial\psi/\partial x)$ are the velocity components. Equations (2*a, b*) imply that the production of thermal and haline variances is balanced – in a statistically steady state – by their molecular dissipation. Equation (2*c*) states that the difference between the potential energy lost by the salt component and the energy gained by the thermal stratification is converted into kinetic energy and ultimately dissipated by molecular viscosity. Other quantities of interest are the flux ratio

$$\gamma = \frac{\langle w\alpha T \rangle}{\langle w\beta S \rangle}, \quad (3)$$

which has to be less than unity to satisfy the principle of energy conservation, and the Nusselt number

$$Nu = \frac{\langle wT \rangle}{-k_T \partial \bar{T} / \partial z}, \quad (4)$$

the ratio of the vertical eddy and molecular fluxes of heat.

The key non-dimensional numbers governing the evolution of system (1) are the Prandtl number $Pr = \nu/k_T$, the diffusivity ratio $\tau = k_S/k_T$, and the background density ratio R_ρ . As mentioned earlier, we are concerned here with the local flux–gradient laws. We assume that, in the absence of large-scale structures, the boundary conditions have a minor influence on the interior circulation. Thus, fluxes are independent of the non-dimensional parameters related to the domain size (e.g. the Rayleigh number). The local flux–gradient laws are commonly used to parameterize the effects of salt fingering on the oceanic circulation (e.g. Kunze 2003) and attempts have been made to validate the concept of an ‘unbounded T – S gradient’. For instance, Radko & Stern (1999) examined the sensitivity of salt-finger fluxes to the domain height (H). A series of numerical simulations with periodic boundary conditions, in which H was varied by an order of magnitude, resulted in virtually no systematic change in the fluxes.† These calculations emphasized the importance of the local gradients in controlling the salt-finger temperature and salinity transport. Of course, before applying the flux–gradient laws to double-diffusive systems, each case should be examined with caution to ensure that there is enough scale separation between the background patterns and salt fingers to justify the “unbounded T – S gradient” model.

To gain a preliminary understanding of the unbounded salt-finger system and its dependence on (R_ρ, τ, Pr) , equations (1) were solved numerically using a fully dealiased pseudospectral method described in Stern & Radko (1998). In the following calculation, we use a diffusivity ratio of $\tau = 1/3$ which is higher than the heat/salt value ($\tau = 1/100$). This choice is dictated by numerical convenience – otherwise it becomes

† We note that the double-diffusive flux laws are very different from those in turbulent convection, where transport is always controlled by the Rayleigh number. The difference is attributed to the distinct range of spatial scales of salt fingers, which permits their scale separation from the background large-scale patterns.

necessary to resolve the very small scales set by dissipation of salt. Nevertheless, as discussed in Stern *et al.* (2001), such a modification is not expected to alter the fundamental physics and dynamics of salt fingering. The Prandtl number is $Pr = 7$, and the numerical experiment (figure 1a) was performed with the overall density ratio of $R_\rho = 1.8$. The size of the computational domain corresponds to 10×10 fastest growing (on the basic gradient) finger wavelengths (d). The flow was resolved by a uniform mesh with $(N_x \times N_z) = (1024 \times 1024)$ elements, and the model was initialized from rest by a small-amplitude random computer-generated initial (T, S) distribution. After a few characteristic growth periods, active statistically steady double-diffusive convection was established. Figure 1(a) shows the instantaneous salinity field which exhibits typical signatures (e.g. Stern *et al.* 2001) of a fully developed field of two-dimensional salt fingers. The Nusselt number, measuring the intensity of salt fingering, is $Nu = 7.1$.

Figure 1(b) shows the numerical experiment performed with the density ratio $R_\rho = 1.2$; as previously, $(\tau, Pr) = (\frac{1}{3}, 7)$ and the computational domain resolves ten fastest growing finger wavelengths in x and z . However a visual comparison of the two experiments in figure 1 reveals that the pattern of salt fingering at low density ratio is much more complex and disorganized. The fully developed temperature field in figure 1b exhibits a much wider range of spatial scales and the Nusselt number increases to $Nu = 77$. In addition to its space-time complexity, the $R_\rho \rightarrow 1$ regime is also characterized by the appearance of coherent dipolar eddies (double-diffusive modons) which translate vertically while roughly preserving their form and T - S anomalies. One of the modons is shown in figure 2 which presents an enlarged view of the small square area marked in figure 1(b). The patterns of temperature and salinity in figures 2(a,b) indicate that the modon is roughly circularly symmetric; the T - S anomalies reach their maximum values at its centre and reduce to zero at the edge. As indicated by the distribution of vorticity in figure 2(c), the interior circulation consists of two symmetric closely packed counter-rotating patches – hence the term double-diffusive modon. Vorticity is also spatially localized, reducing to zero towards the modon edge. The velocity distribution in the modon's interior is shown in figure 2(d).

2.2. Spatial scales of fully developed salt fingering

A well-documented property of salt fingering is related to the strong dependence of temperature and salinity fluxes on the density ratio (see the reviews of Kunze 2003, and Schmitt 2003, for a summary of laboratory, numerical, and observational flux measurements). It is particularly relevant for our discussion to emphasize the extremely high values of the Nusselt number (Nu) for the density ratio close to one. $R_\rho = 1$ corresponds to a homogeneous background density distribution – the boundary between salt fingering and top-heavy convection. Thus, for R_ρ approaching unity, the background density gradient weakens and becomes ineffective in limiting the vertical eddy transport, causing Nu to increase dramatically. These tendencies will be rationalized by the analytical solutions in this paper (§4), which suggest that the Nusselt number approaches infinity for $R_\rho \rightarrow 1^+$.

The condition

$$Nu \gg 1 \text{ for } R_\rho \rightarrow 1^+ \quad (5)$$

has important implications for the spatial scales of salt fingers. The scale of the primary salt finger instability – the fastest growing salt-finger width (d) – remains finite for $R_\rho \rightarrow 1$. However, the flow field in this limit develops a wide range of

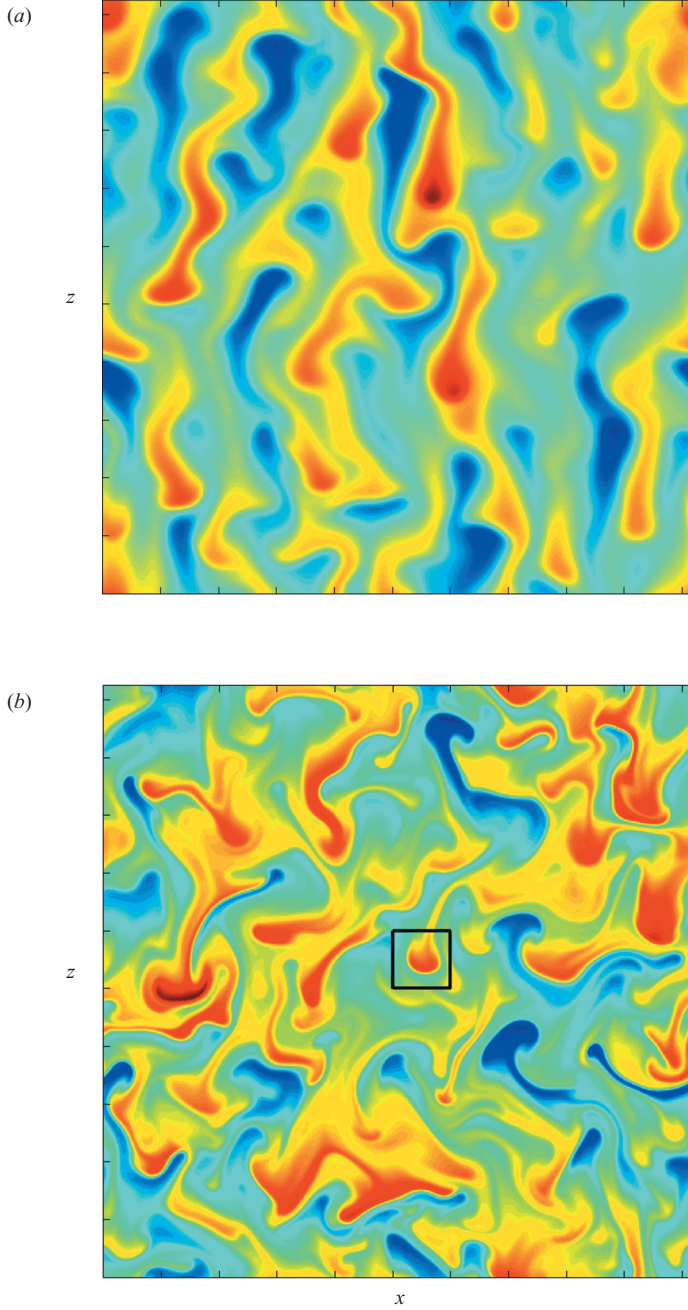


FIGURE 1. Instantaneous salinity fields for the numerical experiments with (a) $R_\rho = 1.8$ and (b) $R_\rho = 1.2$. In both cases $\tau = \frac{1}{3}$ and $Pr = 7$. Red colour corresponds to high values of S and low values are shown in blue. Note the appearance of coherent isolated plumes in (b).

smaller scales: figure 1(b) ($R_\rho = 1.2$) reveals the presence of eddies with dimensions considerably less than d .

The appearance of small scales in the low-density-ratio regime can be rationalized by the following argument, not unlike that of classical turbulence theory. Suppose for

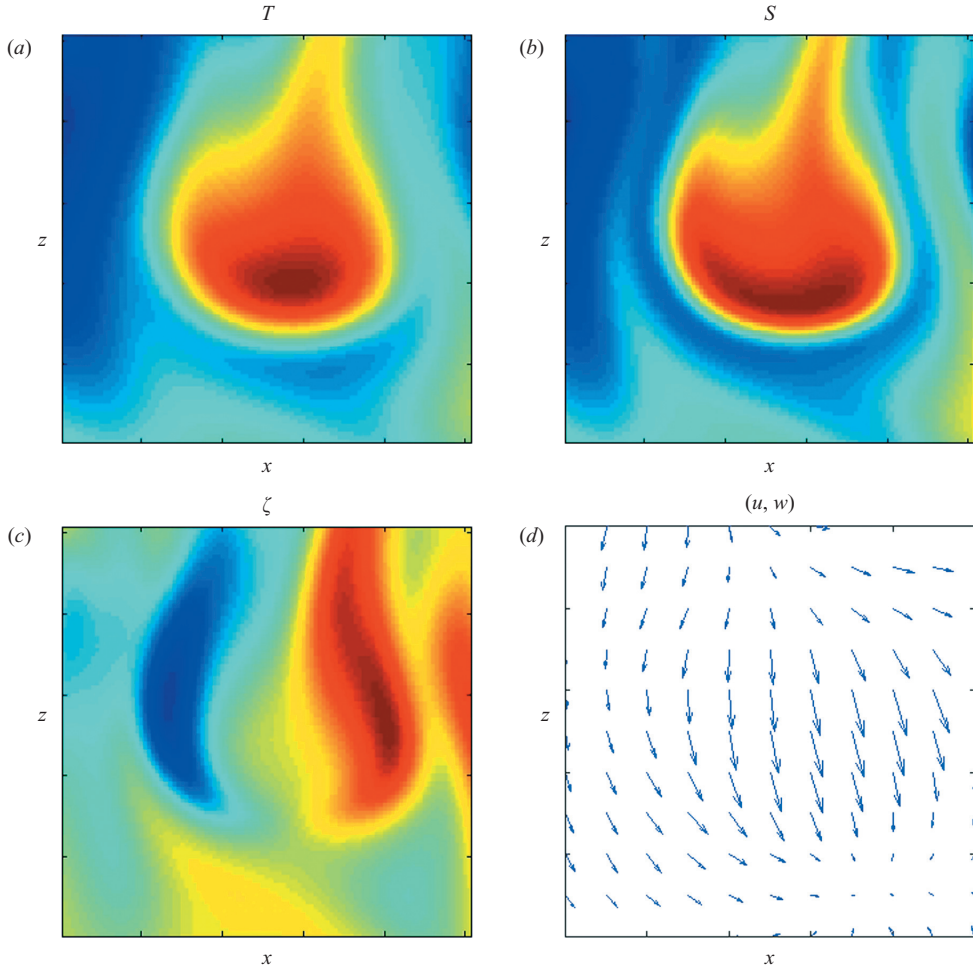


FIGURE 2. An enlarged view of the square area marked in figure 1(b) which contains a well-defined double-diffusive modon. Presented are (a) temperature, (b) salinity, (c) vorticity, and (d) velocity fields. Red colour corresponds to positive values and negative values are shown in blue.

a moment that all relevant scales in the $R_\rho \rightarrow 1$ limit are comparable to the fastest growing finger width d . Since the amplitudes of temperature and velocity increase for density ratio approaching unity, the nonlinear advection term $J(\psi, T)$ inevitably exceeds the diffusive term $k_T \nabla^2 T$:

$$\frac{J(\psi, T)}{k_T \nabla^2 T} \sim \frac{\{v\}\{T\}}{k_T \{T\}/d} \sim Nu, \quad (6)$$

where $\{v\}$ and $\{T\}$ are the scales of the velocity and temperature. In view of (5) and (6), one is naively tempted to neglect the diffusive term for $R_\rho \rightarrow 1$, which immediately leads to a paradox. According to equation (2a), it is the diffusive term that balances the temperature flux associated with active salt fingering; if the diffusive term is negligible, there is nothing to balance the production of thermal variance. The logical resolution of this paradox is that our initial assumption is not valid – not all scales are of the order d . The secondary instabilities of the primary salt fingers generate smaller scales, which in turn transfer motion to even smaller scales, and so forth,

down to the microscales $\lambda_T, \lambda_S \ll d$ at which heat and salt are efficiently dissipated by the molecular diffusivity. This process is a direct counterpart of the cascade of energy and tracer variance to smaller and smaller scales in turbulence problems. However, there is one feature which distinguishes the salt fingering at $R_\rho \rightarrow 1$ from the more common forms of turbulence: the absence of the upscale cascade of energy (Batchelor 1969). Even though all our numerical simulations (figure 1) are two-dimensional, they reveal no evidence of the spontaneous generation of large-scale structures.

A question that naturally arises at this stage is what determines the dissipative scale. Following the conventional argument of turbulence theory (e.g. Monin & Ozmidov 1985), we assume that the cascade of T - S variances to small scales and their dissipation scales are controlled by the supply of energy at the scale of primary instability (d). The balance of energy includes three major components: the loss of potential energy of the salt stratification $D_S = g\langle w\beta S \rangle$, the gain of energy by the temperature $D_T = g\langle w\alpha T \rangle$, and production of kinetic energy $D_v = D_S - D_T$. Fortunately, all three components are of the same order: Numerical simulations (Stern *et al.* 2001) and theoretical arguments (Schmitt 1979) suggest that the flux ratio (3) is finite and less than unity in the limit $R_\rho \rightarrow 1$:

$$0 < \gamma_0 < 1, \quad \gamma_0 = \lim_{R_\rho \rightarrow 1} \gamma, \quad (7)$$

and therefore $D_T = \gamma_0 D_S$, $D_v = (1 - \gamma_0) D_S$, and D_S are comparable:

$$D_S \sim D_T \sim D_v. \quad (8)$$

If the dissipation scale is not strongly affected by the background stratification, then the dimensional arguments require that λ_T is set by the Batchelor microscale

$$\lambda_T \sim \left(\frac{\nu k_T^2}{D_T} \right)^{1/4}. \quad (9)$$

The latter is equivalent to the Kolmogorov scale for Prandtl number of order one. In terms of the Nusselt number (Nu), (9) can be written as

$$\frac{\lambda_T}{l} \sim Nu^{-1/4} \quad \text{for } Nu \gg 1, \quad (10)$$

where $l = (k_T \nu / (g\alpha \bar{T}_z))^{1/4}$ is a length scale based on the background stratification.

To test (10), we performed a series of experiments with $R_\rho = 1.1, 1.2, 1.3, 1.4$, and 1.5 in which the diffusivity ratio was kept constant at $\tau = \frac{1}{3}$ and the Prandtl number was $Pr = 7$. In each case the model was initialized from rest by a small-amplitude random initial (T, S) distribution, on a domain of size resolved 10×10 fastest growing finger wavelengths (d), and the model runs were extended into the quasi-equilibrium regime with statistically steady integral characteristics. For each run, we use the periodically recorded fields of temperature to construct $P_T(\kappa)$, which is the two-dimensional dissipation spectrum of αT and $\kappa = \sqrt{k_x^2 + k_z^2}$ is a wavenumber. For each R_ρ , the dissipation scale (λ_T) is plotted (figure 3) as a function of Nu . The dissipation scale is determined by fitting the Batchelor (1959) dissipation spectrum to $P(\kappa)$ and defining

$$\lambda_T = \frac{2\pi}{\kappa_B} \quad (11)$$

where κ_B is the Batchelor wavenumber. The slope of the numerical $\lambda_T(Nu)$ relation in the logarithmic coordinates (figure 3) is consistent with the power law (10).

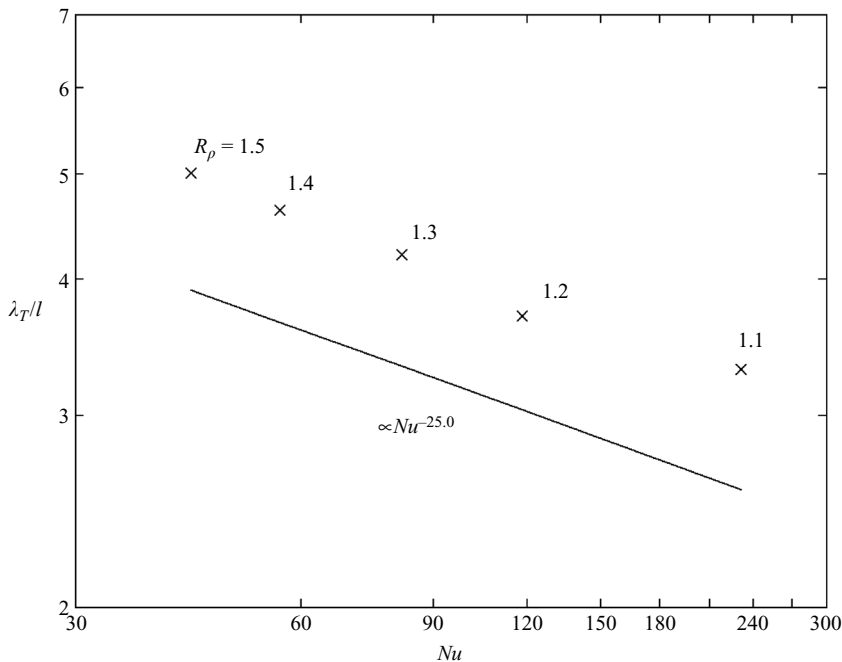


FIGURE 3. The non-dimensional heat dissipation scale (λ_T/l) as a function of the Nusselt number (Nu) in logarithmic coordinates. All data points (denoted by crosses) are aligned along a straight line whose slope corresponds to a power law $\lambda_T/l \propto Nu^{-0.25}$.

It is also possible to refine the foregoing analysis by introducing different dissipation scales for the individual density components. Since we expect comparable dissipation rates for heat and salt in (2), the salt dissipation scale (λ_S) should differ from the dissipation scale of heat by a factor $\sqrt{\tau} = \sqrt{k_S/k_T}$:

$$\lambda_S = \sqrt{\tau} \lambda_T, \quad (12)$$

yet another rather conventional prediction, consistent with all our numerical experiments. In figure 4 we present the dissipation spectra for the $R_\rho = 1.2$ calculation in figure 1(b). $P_T(\kappa)$ and $P_S(\kappa)$ are the dissipation spectra of $(\alpha T, \beta S)$, normalized by $P_{\max} = \max_k \{P_S(\kappa)\}$. We note the remarkably similar patterns of the T - S spectra, which we demonstrate by renormalizing the temperature spectrum as

$$\kappa' = \kappa \sqrt{\tau}, \quad P'_T = P_T \frac{\sqrt{\tau}}{\gamma R_\rho}, \quad (13)$$

and plotting $P'_T(\kappa')$ in figure 4 (dashed curve). $P'_T(\kappa')$ is almost undistinguishable from $P_S(\kappa)$ over much of the κ -range, which is consistent with the shift of the salinity dissipation scales relative to that of temperature by a factor $\sqrt{\tau}$, as anticipated in (12).

As mentioned earlier, simulations reveal the abundance of compact isolated blobs propagating vertically while roughly preserving their shape and distribution of temperature and salinity (see figures 1, 2) – the double-diffusive modons. In order to preserve the T - S anomalies in time, vertical advection of properties in modons should be balanced by their molecular dissipation. In particular, $w \partial \bar{S} / \partial z \sim k_S \nabla^2 S$, which implies that on the modon scale, advective and dissipative terms in the

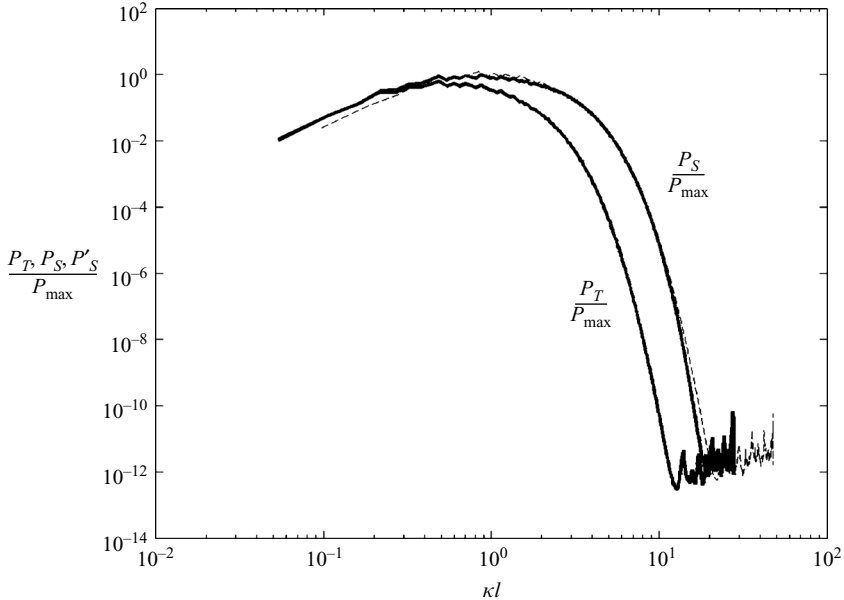


FIGURE 4. The dissipation spectra of temperature (P_T) and salinity (P_S) normalized by the maximum of the salinity dissipation spectra (P_{\max}). The dashed curve (P'_T) represents the temperature dissipation rescaled according to (13). The $P'_T(\kappa)$ and $P_S(\kappa)$ curves are nearly identical.

salinity equation are comparable. Thus, we interpret double-diffusive modons as fundamentally diffusive structures operating on the salinity microscale λ_S , which is consistent with the range of scales observed in the numerical simulations (figure 1). Indeed, on scales greatly exceeding λ_S , molecular diffusion is negligible and all coherent density anomalies just oscillate about the equilibrium level. On scales much less than λ_S , the perturbations are rapidly obliterated by the molecular diffusion. This leaves only one possibility: the modon size should be comparable to λ_S . As far as the dissipation of heat is concerned, we note that T -anomaly within the modon interior is small and only slightly affects the density distribution.

On the other hand, since modons are reflected in both temperature and salinity distributions, we anticipate that spacing between modons is set by the heat dissipation scale λ_T . These conjectures are supported by the numerical experiments in figure 5, which shows the typical instantaneous salinity fields realized for (a) $\tau = \frac{1}{3}$ and (b) $\tau = \frac{1}{12}$. Both experiments were performed with $(R_\rho, Pr) = (1.3, 7)$ and on a resolved domain of size 10×10 fastest growing finger wavelengths. The time-mean Nusselt number realized in the $\tau = \frac{1}{3}$ simulation was $Nu = 47.4$ and for $\tau = \frac{1}{12}$ it increased to $Nu = 82.5$. The experiments in figures 5(a) and 5(b) resulted in a comparable number of structures that we can identify as double-diffusive modons; their concentration increased by only $\sim 50\%$ for the $\tau = \frac{1}{12}$ calculation, which we attribute to its larger Nusselt number (see (10)). However the size of individual modons changed dramatically. The typical scale of modons in figure 5(b) is less than half of that in figure 5(a) and it is well separated from the scale of the primary instability. The salinity dissipation scale λ_S is represented by the radius of the black circle plotted in the lower right corners of figure 5(a,b). In each experiment, the typical size of modons is comparable to λ_S .

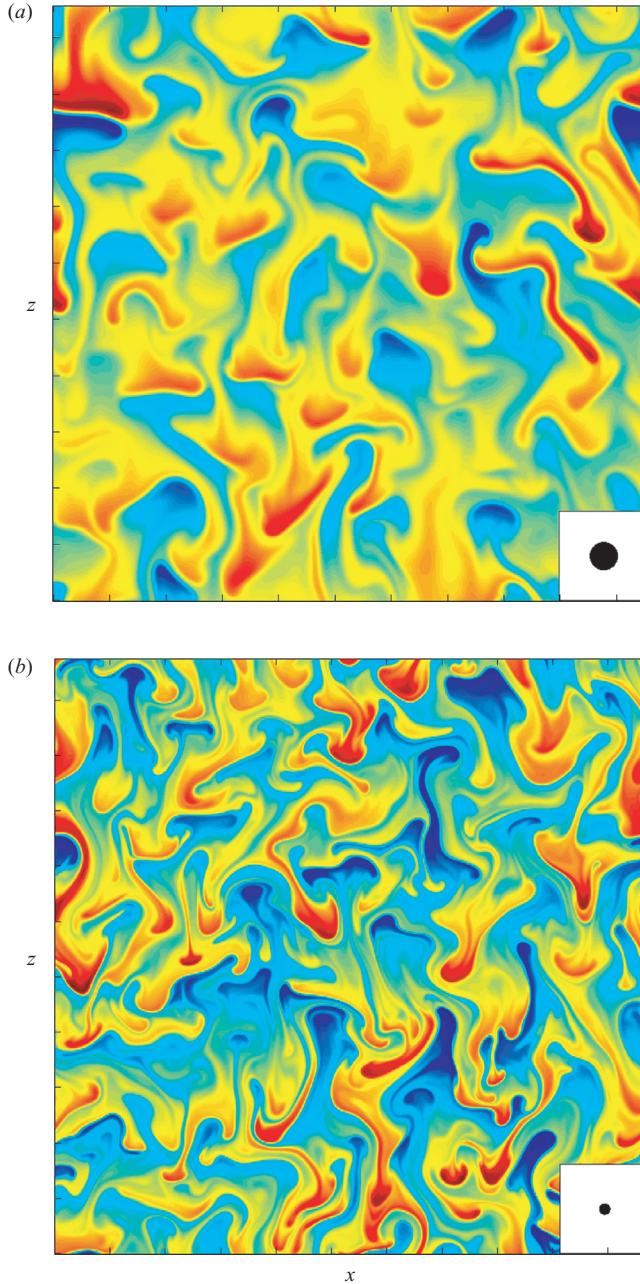


FIGURE 5. Instantaneous salinity fields for the experiments with (a) $\tau = \frac{1}{3}$ and (b) $\tau = \frac{1}{12}$. In both cases $R_\rho = 1.3$ and $Pr = 7$. Red colour corresponds to high values of S and low values are shown in blue. Note the dramatic reduction in size of the double-diffusive modons in (b). The radii of the black circles at the right bottom corners in (a) and (b) represent the salinity dissipative scale (λ_S).

In view of their scales ($R \sim \lambda_S \ll \lambda_T$), we presume that modons account for only a fraction of the total heat dissipation and thus for a fraction of heat flux. In contrast, dissipation of the salinity occurs mostly on the λ_S scale – the scale of modons –

and therefore it is sensible to attribute the salt flux to the action of double-diffusive modons. Our study will consequently emphasize the modon-driven mixing of the slower diffuser – salt. If the modon size is of the order of λ_S and the typical distance from one modon to its closest neighbour is of the order of λ_T , then (12) implies that the fraction of the total area (A_{total}) occupied by double-diffusive modons (A_{mod}) is proportional to the diffusivity ratio τ :

$$\frac{A_{mod}}{A_{total}} \propto \tau. \quad (14)$$

As τ decreases, modons become more and more isolated, and yet they continue to account for the major part of salt dissipation.

Of course, the flow patterns observed in the numerical simulations (figures 1, 2, and 5) are not limited to double-diffusive modons: salt-finger convection exhibits a rich array of more irregular and short-lived structures. Narrow filaments trailing behind – and the sharp fronts forming ahead of – the propagating modons are ubiquitous, and so are the larger wave-like perturbations. These less-coherent eddies may also contribute to the overall dissipation of salt. However, it is our belief that many gross features of double-diffusive convection can be explained by focusing exclusively on the dynamics and transport of the double-diffusive modons. This belief will be profitably explored in formulating, and successfully testing, the mixing model based on the analytical solution for individual modons – a solution that we describe next.

3. The double-diffusive modon

Numerical simulations exhibit the emergence of rectilinearly propagating dipolar structures (figure 2) and motivate a search for the corresponding analytical similarity solutions. These solutions represent each modon as an isolated, horizontally symmetric, circular eddy with a compact distribution of T – S in the interior. The explicit expressions for temperature, salinity, and streamfunction are derived by requiring the flow to be steady in the coordinate system associated with the moving modon. We also impose the condition of no advective flux across the modon boundary. This condition implies that the modon transports with it all fluid trapped in its interior, analogous to that in the classical modon theory (Stern 1975a; Larichev & Reznik 1976).

3.1. Formulation

The governing equations (1) are non-dimensionalized using $l = (k_T \nu / g \alpha \bar{T}_z)^{1/4}$, k_T/l , and l^2/k_T as the scales of length, velocity, and time respectively. The expansion/contraction coefficients (α , β) are incorporated in (T, S) , and $\alpha \bar{T}_z l$ is used as the scale for both temperature and salinity perturbations, resulting in

$$\left. \begin{aligned} \frac{\partial T}{\partial t} + J(\psi, T) + \frac{\partial \psi}{\partial x} &= \nabla^2 T, \\ \frac{\partial S}{\partial t} + J(\psi, S) + \frac{1}{R_\rho} \frac{\partial \psi}{\partial x} &= \tau \nabla^2 S, \\ \frac{\partial}{\partial t} \nabla^2 \psi + J(\psi, \nabla^2 \psi) &= Pr \left[\frac{\partial}{\partial x} (T - S) + \nabla^4 \psi \right]. \end{aligned} \right\} \quad (15)$$

The perturbation density in non-dimensional units becomes $\rho = S - T$.

To describe the uniformly translating structures, as observed in the numerical simulations, we rewrite the equations of motion in a coordinate system which moves

vertically with the speed W :

$$\frac{\partial}{\partial t} \rightarrow \frac{\partial}{\partial t} - W \frac{\partial}{\partial z}, \quad \psi \rightarrow \psi + Wx, \quad (16)$$

and insist that the flow field in the new coordinate system is steady:

$$\left. \begin{aligned} W + J(\psi, T) + \frac{\partial \psi}{\partial x} &= \nabla^2 T, \\ \frac{W}{R_\rho} + J(\psi, S) + \frac{1}{R_\rho} \frac{\partial \psi}{\partial x} &= \tau \nabla^2 S, \\ J(\psi, \nabla^2 \psi) &= Pr \left[\frac{\partial}{\partial x} (T - S) + \nabla^4 \psi \right]. \end{aligned} \right\} \quad (17)$$

For convenience, we also use the total temperature and salinity, which includes the contributions from the basic gradient $T_{tot} = T + z$ and $S_{tot} = S + z/R_\rho$. This transformation further reduces our governing equations to

$$\left. \begin{aligned} W + J(\psi, T_{tot}) &= \nabla^2 T_{tot}, \\ \frac{W}{R_\rho} + J(\psi, S_{tot}) &= \tau \nabla^2 S_{tot}, \\ J(\psi, \nabla^2 \psi) &= Pr \left[\frac{\partial}{\partial x} (T_{tot} - S_{tot}) + \nabla^4 \psi \right]. \end{aligned} \right\} \quad (18)$$

Since our goal is to understand the limit $R_\rho \rightarrow 1^+$, we now introduce a small parameter $\varepsilon = \sqrt{1 - R_\rho^{-1}}$ and search for a solution of the governing equations by expanding (T, S, ψ) in powers of ε . Suppose that the leading-order scale of temperature and salinity of double-diffusive modons is $T_{tot}, S_{tot} \sim \varepsilon^q$, and the typical spatial scale of the modon is $\Delta x, \Delta y \sim \varepsilon^p$ where the exponents q and p are yet to be determined. Thus, the dissipation of thermal variance is of the order of $D_T = \langle |\nabla T|^2 \rangle \sim \varepsilon^{2q-2p}$ and (10) therefore implies that $\varepsilon^p \sim (1/\varepsilon^{2q-2p})^{1/4}$; consequently $p = -q > 0$. Thus, the spatial coordinates are rescaled as

$$x = \varepsilon^p x_0, \quad z = \varepsilon^p z_0. \quad (19)$$

The scale for the propagation velocity is determined by requiring W to be of the same order as the diffusive term in the T - S equations:

$$W = \varepsilon^{-3p} W_0 + \dots \quad (20)$$

Our preliminary numerical simulations in §2 suggest looking for a solution confined to a circular region with a symmetric distribution of temperature and salinity:

$$\left. \begin{aligned} T_{tot} &= \varepsilon^{-p} T_0(r) + \dots, \\ S_{tot} &= \varepsilon^{-p} S_0(r) + \dots, \end{aligned} \right\} \quad (21)$$

where, for convenience, we have switched to the polar coordinates (r, θ) such that $x_0 = r \cos \theta$ and $z_0 = r \sin \theta$. Anticipating the balance between the buoyancy and viscous terms in the vorticity equation, which implies that $\nabla^4 \psi \approx -(\partial/\partial x)(T - S) \approx \varepsilon^{-2p}(\partial/\partial r)(S_0 - T_0) \cos \theta$, we use the following leading-order term for the streamfunction:

$$\psi = \varepsilon^{2p} \psi_0(r) \cos \theta + \dots \quad (22)$$

Note that (22) represents the motion of particles relative to the modon, and it is much slower than the propagation velocity of the modon itself (20). In essence, the scaling (22) represents the variation in velocities in the modon interior, rather than their

absolute values. While the scale separation between the propagation velocity of the modon and the velocity variation in its interior is perhaps somewhat counterintuitive, this feature is reflected in the numerical simulations. Figure 2(d) indicates that the particle velocities are fairly uniform in the central part of the modon. Scaling (22) also implies that the nonlinear terms in T - S equations (18) do not appear at their leading ($\sim \varepsilon^{-3p}$) order, which reduces these equations to

$$\left. \begin{aligned} W_0 &= \frac{\partial^2 T_0}{\partial r^2} + \frac{1}{r} \frac{\partial T_0}{\partial r}, \\ W_0 &= \tau \left(\frac{\partial^2 S_0}{\partial r^2} + \frac{1}{r} \frac{\partial S_0}{\partial r} \right). \end{aligned} \right\} \quad (23)$$

Since the propagation velocity is likely to be affected by the external drag force, it also becomes necessary to specify the response of the exterior to the motion of the double-diffusive modon. The theory of propagation through a surrounding viscous fluid has a long and distinguished history (see Schlichting & Gersten 2000). While details are still debated, it is generally accepted that the drag force acting on a blunt solid object moving through a motionless viscous fluid is controlled by the Reynolds number $Re = W * R^*/\nu$, where W^* is the dimensional propagation velocity and R^* is the spatial scale. When the Reynolds number is small, the external force is dominated by the frictional drag, which is proportional to the speed of the object. For large Reynolds numbers, the pressure (form) drag becomes more significant and the external force is proportional to the velocity squared. Of course, the double-diffusive problem contains many ingredients that are absent in the classical solid-body propagation theory. The modon interior is not rigid and the diffusion of heat and salt across its boundary adds another element of complexity. Nevertheless, it is sensible to assume from the outset that the drag laws realized for blunt solid objects are relevant for double-diffusive modons as well.

The Reynolds number based on the modon propagation velocity is large – in our non-dimensional units $Re = WR/Pr$, and in view of (19) and (20) $Re \sim \varepsilon^{-2p} \gg 1$.[†] For the modon in figure 2, we have explicitly computed the form (F_p) and viscous (F_v) drag components and found that $F_p/F_v = 2.83$. Therefore, we adopt the quadratic drag law:

$$F = CW^2, \quad (24)$$

and the following theory can be readily reproduced for other forms of F , should such be proposed for double-diffusive modons. The coefficient C in (24) depends on the modon size and on the pattern of exterior motion, both of which are determined by the background density ratio. Even the shape of modons in the numerical simulations, but not in the theory, may be affected by the background density ratio. Therefore we anticipate that C in (24) is related to R_ρ in some, yet unspecified, manner: $C = C(R_\rho)$. Since the propagation velocity does not vary in time, the drag experienced by the modon is balanced by its buoyancy – the Archimedes force measuring the excess

[†] The Reynolds number based on the propagation speed, which is used here for selection of the drag law, should be clearly distinguished from the Reynolds number based on the scale of the interior particle velocities relative to the moving modon. Note that the modons are dissipative structures and therefore the Reynolds and Péclet numbers based on the interior velocity are necessarily of order one. This interior Reynolds number, however, is irrelevant for the estimate of the external drag force.

weight of the modon with respect to the background density, and therefore

$$\iint_{r < R} (S - T) dx dy = -CW^2. \quad (25)$$

Equation (25) connects the interior and exterior dynamics and makes it possible to close the problem and to determine the basic characteristics of the double-diffusive modons as a function of R_ρ . In order to make (25) consistent with the scaling in (19)–(21), we require that

$$C = C_0 \varepsilon^{7p}. \quad (26)$$

Our purpose here is to represent the configuration with finite temperature and salinity confined to a circular area $r < R$, outside which our solution decreases to zero. However, before presenting specific solutions, we note that our governing equations (18) are invariant under the transformation:

$$\left. \begin{aligned} (x_0, z_0) &\rightarrow R(x_0, z_0), & (u, w) &\rightarrow \frac{1}{R}(u, w), & \psi &\rightarrow \psi, \\ (T_{tot}, S_{tot}) &\rightarrow \frac{1}{R^3}(T_{tot}, S_{tot}), & W &\rightarrow \frac{1}{R^5}W. \end{aligned} \right\} \quad (27)$$

Thus, we can, without loss of generality, consider only the reference case of a double-diffusive modon with rescaled radius of unity and determine its vertical speed (W). The propagation velocity of a modon with arbitrary radius R will be determined by dividing the reference value W by R^5 .

3.2. Nonlinear asymptotic expansion

For the modon of unit radius, (23) requires the following zero-order T – S fields:

$$\left. \begin{aligned} T_0 &= \frac{W_0}{4}(r^2 - 1) \\ S_0 &= \frac{W_0}{4\tau}(r^2 - 1) \end{aligned} \right\} \text{for } r < 1. \quad (28)$$

The leading-order ($\sim \varepsilon^{-2p}$) balance of the vorticity equation yields

$$0 = \frac{\partial}{\partial r} (T_0 - S_0) + \left(\frac{\partial^2}{\partial r^2} + \frac{1}{r} \frac{\partial}{\partial r} - \frac{1}{r^2} \right)^2 \psi_0. \quad (29)$$

Equation (29) is solved by introducing the vorticity $\zeta = \nabla^2 \psi$, whose zero-order component $\zeta_0 \cos(\theta)$ satisfies

$$\zeta_0 = \left(\frac{\partial^2}{\partial r^2} + \frac{1}{r} \frac{\partial}{\partial r} - \frac{1}{r^2} \right) \psi_0.$$

To determine ζ_0 , it becomes necessary to specify the boundary conditions; these are introduced by insisting that the vorticity has no singularities in the interior and that it reduces to zero at the boundary of the modon ($r = 1$):

$$\zeta_0 = \frac{W_0}{16} \left(\frac{1}{\tau} - 1 \right) r[r^2 - 1]. \quad (30)$$

From (30) we similarly compute the zero-order streamfunction:

$$\psi_0 = \frac{W_0}{384} \left(\frac{1}{\tau} - 1 \right) r[r^2 - 1][r^2 - 2]. \quad (31)$$

The nonlinear interaction of the leading-order terms ((21) and (22)) in the advection–diffusion equations (18) generates T – S modes proportional to $\sin \theta$:

$$\left. \begin{aligned} T_{tot} &= \varepsilon^{-p} T_0(r) + \varepsilon^p T_1(r) \sin \theta + \dots, \\ S_{tot} &= \varepsilon^{-p} S_0(r) + \varepsilon^p S_1(r) \sin \theta + \dots, \end{aligned} \right\} \quad (32)$$

and the nonlinearity of the vorticity equation (18) generates a streamfunction mode proportional to $\sin 2\theta$:

$$\psi = \varepsilon^{2p} \psi_0(r) \cos \theta + \varepsilon^{4p} \psi_1(r) \sin 2\theta + \dots. \quad (33)$$

Collecting the first-order terms of the advection–diffusion equations ($\sim \varepsilon^{-p}$) and of the vorticity equation (~ 1), we arrive at

$$\left. \begin{aligned} \frac{\psi_0}{r} \frac{\partial T_0}{\partial r} &= \left(\frac{\partial^2}{\partial r^2} + \frac{1}{r} \frac{\partial}{\partial r} - \frac{1}{r^2} \right) T_1, \\ \frac{\psi_0}{r} \frac{\partial S_0}{\partial r} &= \tau \left(\frac{\partial^2}{\partial r^2} + \frac{1}{r} \frac{\partial}{\partial r} - \frac{1}{r^2} \right) S_1, \\ \frac{\psi_0}{r} \frac{\partial \underline{s}_0}{\partial r} - \frac{\partial \psi_0}{\partial r} \frac{\underline{s}_0}{r} &= Pr \left[\frac{\partial(T_1 - S_1)}{\partial r} - \frac{T_1 - S_1}{r} + 2 \left(\frac{\partial^2}{\partial r^2} + \frac{1}{r} \frac{\partial}{\partial r} - \frac{4}{r^2} \right)^2 \psi_1 \right]. \end{aligned} \right\} \quad (34)$$

The nonlinear interaction of the zero- and first-order terms (32) and (33) in the advection–diffusion equations (18) generates two types of T – S modes: those proportional to $\cos 2\theta$ and those independent of θ ,

$$\left. \begin{aligned} T_{tot} &= \varepsilon^{-p} T_0(r) + \varepsilon^p T_1(r) \sin \theta + \varepsilon^{3p} T_{20}(r) + \varepsilon^{3p} T_{22}(r) \cos 2\theta + \dots, \\ S_{tot} &= \varepsilon^{-p} S_0(r) + \varepsilon^p S_1(r) \sin \theta + \varepsilon^{3p} S_{20}(r) + \varepsilon^{3p} S_{22}(r) \cos 2\theta + \dots. \end{aligned} \right\} \quad (35)$$

The nonlinear interaction of the zero- and first-order terms in the vorticity equation also generates two types of terms – modes proportional to $\cos \theta$ and $\cos 3\theta$:

$$\psi = \varepsilon^{2p} \psi_0(r) \cos \theta + \varepsilon^{4p} \psi_1(r) \sin 2\theta + \varepsilon^{6p} \psi_{21}(r) \cos \theta + \varepsilon^{6p} \psi_{23}(r) \cos 3\theta + \dots. \quad (36)$$

Next, we collect the second-order ($\sim \varepsilon^p$) θ -independent terms of the T – S equations. The spatially uniform terms W and W/R_ρ in (18), associated with vertical translation of the double-diffusive modon, are also taken into account and expanded as follows:

$$\left. \begin{aligned} W &= \varepsilon^{-3p} W_0 + \varepsilon^p W_2, \\ W/R_\rho &= W(1 - \varepsilon^2) = \varepsilon^{-3p} W_0 - \varepsilon^{-3p+2} W_0 + \varepsilon^p W_2 - \varepsilon^{p+2} W_2. \end{aligned} \right\} \quad (37)$$

In constructing the modon solution, we insist that the background density gradient (the $\varepsilon^{-3p+2} W_0$ term) explicitly influences only the high-order terms. Thus, our second-order equations become

$$\left. \begin{aligned} W_2 + N_{T2} &= \left(\frac{\partial^2}{\partial r^2} + \frac{1}{r} \frac{\partial}{\partial r} \right) T_{20}, \\ W_2 + N_{S2} &= \tau \left(\frac{\partial^2}{\partial r^2} + \frac{1}{r} \frac{\partial}{\partial r} \right) S_{20}, \\ N_{\psi 2} &= Pr \left[\frac{\partial(T_{20} - S_{20})}{\partial r} + \left(\frac{\partial^2}{\partial r^2} + \frac{1}{r} \frac{\partial}{\partial r} - \frac{1}{r^2} \right)^2 \psi_{21} \right], \\ \int_0^1 (S_{20} - T_{20}) r \, dr &= -\frac{C_0}{2\pi} 2W_0 W_2 = \frac{2W_2}{W_0} \int_0^1 (S_0 - T_0) r \, dr, \end{aligned} \right\} \quad (38)$$

where the nonlinear terms (N_T, N_S, N_ψ) are

$$\left. \begin{aligned} N_{T2} &= \frac{1}{2} \left(\frac{\partial \psi_0}{\partial r} \frac{T_1}{r} + \frac{\psi_0}{r} \frac{\partial T_1}{\partial r} \right), \\ N_{S2} &= \frac{1}{2} \left(\frac{\partial \psi_0}{\partial r} \frac{S_1}{r} + \frac{\psi_0}{r} \frac{\partial S_1}{\partial r} \right), \\ N_{\psi 2} &= \frac{\partial \psi_0}{\partial r} \frac{\varsigma_1}{r} + \frac{1}{2} \frac{\psi_0}{r} \frac{\partial \varsigma_1}{\partial r} - \frac{1}{2} \frac{\partial \psi_1}{\partial r} \frac{\varsigma_0}{r} - \frac{\psi_1}{r} \frac{\partial \varsigma_0}{\partial r}, \end{aligned} \right\} \quad (39)$$

and

$$\varsigma_1 = \left(\frac{\partial^2}{\partial r^2} + \frac{1}{r} \frac{\partial}{\partial r} - \frac{4}{r^2} \right) \psi_1.$$

A similar set of second-order equations arises for T_{22}, S_{22} , and ψ_{23} .

Next, power series in (35) and (36) are substituted into the governing equations (18) and (25), terms of the same order collected, and the resulting equations are solved for $T_0, T_1, T_{20}, T_{22}, S_0, S_1, S_{20}, S_{22}, \psi_0, \psi_1, \psi_{21}, \psi_{23}, W_2$. For instance, the expression for W_2 is given by

$$W_2 = -\frac{11}{110100480} \frac{\tau^4 - \tau^3 - \tau + 1}{\tau^4} W_0^3, \quad (40)$$

implying that the nonlinear correction to the propagation velocity opposes its zero-order component, a feature that could be expected on physical grounds. Indeed, the nonlinearity in the T - S equations represents the advection of temperature and salinity in the interior of the modon, which accelerates the exchange of properties – from the modon boundary ($r=1$), where $T=S=0$, to its centre ($r=0$), where T and S are maximal. The nonlinear advective transfer tends to reduce the density anomaly of the modon and thereby also reduces the buoyant force (25). Thus, steady-state translation is possible only if the amplitude of the propagation velocity decreases accordingly, as reflected in (40). Note that the appearance of this small correction to the propagation velocity (the W_2 term) is a direct and inevitable consequence of the model dynamics. In the stationary coordinate system, inclusion of the small-amplitude propagation velocity component is equivalent to allowing the slow time scale into the problem and rescaling the time variable as $t = \varepsilon^{4p} t_0 + t_2$.

It should be emphasized that, although the foregoing expansion (which spans orders 0–2 in ε) is nonlinear, the resulting solutions can be found for any value of the propagation velocity W_0 and any positive exponent p . In order to determine their unique preferred values, we now extend our asymptotics to even higher orders.

Extending the power series (35) and (36) to the third and fourth orders, we arrive at

$$\left. \begin{aligned} T_{tot} &= \varepsilon^{-p} T_0(r) + \varepsilon^p T_1(r) \sin \theta + \varepsilon^{3p} T_{20}(r) + \varepsilon^{3p} T_{22}(r) \cos 2\theta + \varepsilon^{5p} T_{31}(r) \sin \theta \\ &\quad + \varepsilon^{5p} T_{33}(r) \sin 3\theta + \varepsilon^{7p} T_{40}(r) + \dots, \\ S_{tot} &= \varepsilon^{-p} S_0(r) + \varepsilon^p S_1(r) \sin \theta + \varepsilon^{3p} S_{20}(r) + \varepsilon^{3p} S_{22}(r) \cos 2\theta \\ &\quad + \varepsilon^{5p} S_{31}(r) \sin \theta + \varepsilon^{5p} S_{33}(r) \sin 3\theta + \varepsilon^{7p} S_{40}(r) + \dots, \\ \psi &= \varepsilon^{2p} \psi_0(r) \cos \theta + \varepsilon^{4p} \psi_1(r) \sin 2\theta + \varepsilon^{6p} \psi_{21}(r) \cos \theta + \varepsilon^{6p} \psi_{23}(r) \cos 3\theta \\ &\quad + \varepsilon^{8p} \psi_{32}(r) \sin 2\theta + \varepsilon^{8p} \psi_{34}(r) \sin 4\theta + \varepsilon^{10p} \psi_{41}(r) \cos \theta + \dots, \\ W &= \varepsilon^{-3p} W_0 + \varepsilon^p W_2. \end{aligned} \right\} \quad (41)$$

As previously, power series in (41) are substituted into the governing equations (18) and (25), terms of the same order collected, and the resulting equations are

solved sequentially. At the fourth-order ($\sim \varepsilon^{5p}$) balance of the salinity equation, we also include the $\varepsilon^{-3p+2}W_0$ term in (37) representing the influence of the background density ratio, which determines a unique value of the exponent p in (41):

$$p = \frac{1}{4}. \quad (42)$$

Attention is now focused on the fourth-order balance of the T - S equations, particularly on its θ -independent harmonic:

$$\left. \begin{aligned} N_{T4} &= \left(\frac{\partial^2}{\partial r^2} + \frac{1}{r} \frac{\partial}{\partial r} \right) T_{40}, \\ -W_0 + N_{S4} &= \tau \left(\frac{\partial^2}{\partial r^2} + \frac{1}{r} \frac{\partial}{\partial r} \right) S_{40}, \end{aligned} \right\} \quad (43)$$

where

$$\left. \begin{aligned} N_{T4} &= \frac{1}{2r} \frac{\partial(\psi_0 T_{31} + \psi_{21} T_1 - 2\psi_1 T_{22})}{\partial r}, \\ N_{S4} &= \frac{1}{2r} \frac{\partial(\psi_0 S_{31} + \psi_{21} S_1 - 2\psi_1 S_{22})}{\partial r}. \end{aligned} \right\} \quad (44)$$

At this point we also make use of the buoyancy–drag balance equation (25), whose fourth-order component yields

$$\int_0^1 (S_{40} - T_{40})r \, dr = -C_0 W_0^2 = \frac{W_0^2}{W_0^2} \int_0^1 (S_0 - T_0)r \, dr. \quad (45)$$

Solving (43) for (T_{40}, S_{40}) and substituting the result in (45) we finally arrive at the equation sought for W_0 :

$$A W_0^4 = B, \quad (46)$$

where A is given by

$$\begin{aligned} A = & [(2164832Pr + 181959784Pr^2 + 127714)\tau^9 + (-6494496Pr - 510856 \\ & - 623552288Pr^2)\tau^8 + (766284 + 4329664Pr + 791141276Pr^2)\tau^7 + (-498997 \\ & - 605669528Pr^2 + 2590252Pr)\tau^6 + (-1350536Pr + 80278 + 584155152Pr^2)\tau^5 \\ & + (71154 - 505281128Pr^2 - 1016888Pr)\tau^4 + (-3924480Pr - 47436 \\ & + 237325164Pr^2)\tau^3 + (-141852280Pr^2 + 5515340Pr + 11859)\tau^2 \\ & + (118886304Pr^2 - 1813688Pr)\tau - 37112456Pr^2] / \\ & (31106318645782904832000Pr^2\tau^9), \end{aligned} \quad (47)$$

and

$$B = -\frac{1}{16\tau}. \quad (48)$$

While (47) seems hopelessly awkward at first, it can be cast in a manageable and physically transparent form by considering the $\tau \ll 1$ limit of the foregoing theory. Thus, in §4 we will develop simple explicit solutions based on the truncated power series in ε and τ .

3.3. Physical interpretation

The individual components of the proposed asymptotic ε -expansion for $\tau = \frac{1}{3}$ and $Pr = 7$ are shown in figure 6. The structure of the equilibrium solution can be physically interpreted by focusing on salinity (S), which controls the density distribution in the modon interior. Consider an upward-propagating modon with relatively fresh and

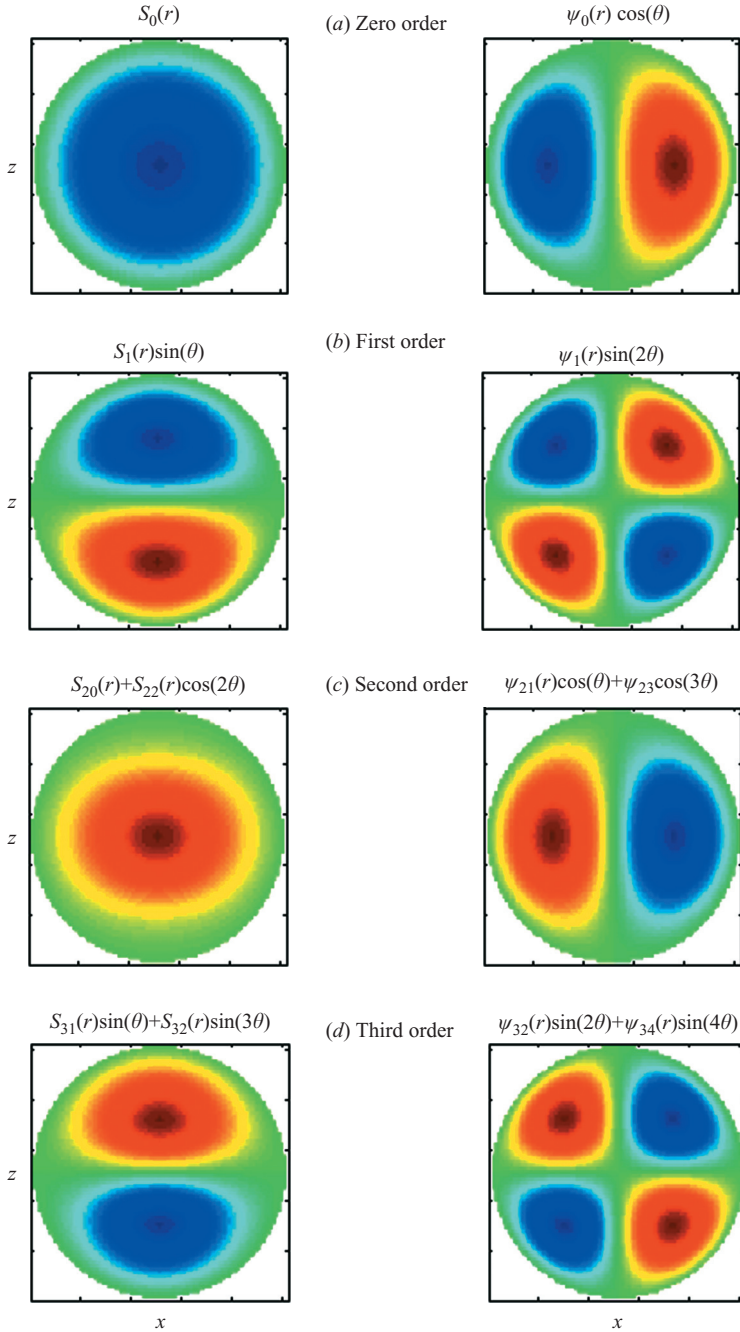


FIGURE 6. The asymptotic solution representing the upward-propagating modon for $\tau = \frac{1}{3}$ and $Pr = 7$. Presented are four leading terms of the ε -expansion (41) for the salinity (left column) and streamfunction (right). Red colour corresponds to positive values and negative values are shown in blue.

cold fluid inside ($W > 0$, $S < 0$). We insist that the governing equations are balanced at all orders in ε . The direct effect of increasing the density ratio above unity (finite ε) would be to reduce the salinity advection term ($W \bar{S}_z$). Indeed, if the temperature

stratification and propagation velocity were fixed, larger density ratio would mean lower background salinity gradient ($\bar{S}_z = \bar{T}_z R_\rho^{-1} = R_\rho^{-1}$) and thus lower mean advection term [$W\bar{S}_z = W\bar{T}_z - W(1 - R_\rho^{-1})$]. What can balance this (weak) tendency in the salinity equation

$$-W(1 - R_\rho^{-1}) < 0 \quad (49)$$

associated with the increase in R_ρ above unity? Another key question is at what order in the ε -expansion can term (49) be balanced.

As indicated by the zero-order salinity distribution (figure 6a, left) density is lowest at the modon centre. An inhomogeneous density distribution drives the dipolar circulation, with light particles in the central part rising faster than the heavy particles near the edge, which is reflected in the pattern of the zero-order streamfunction (figure 6a, right). The induced circulation mixes salinity and thus tends to decrease the salinity amplitude in the modon. Since both processes – advective interior mixing and the background stratification effect (49) – act in the same sense, it is clear that the equilibration cannot be achieved through a simple balance between the variation of a governing parameter (R_ρ in our case) and the leading-order nonlinearity (cf. Malkus & Veronis 1948). Instead, we are forced to delay the inclusion of this \bar{S}_z effect to an even higher order in our ε -expansion. Note that, so far, solutions of any strength could be found.

Since nonlinearity adversely affects the salinity amplitude – the second-order salinity opposes that at the zero order, it is not surprising that the streamfunction follows the same pattern: the second-order streamfunction pattern (figure 6c, left) opposes the zero-order streamfunction (figure 6a, left). Likewise, the third-order circulation pattern (fourth row, left column in figure 6) is anti-correlated with the first-order pattern (figure 6b, left). The resulting reduction in circulation strength, hence the reduction in the advective mixing between the modon boundary and the centre, means that the nonlinearity at the fourth order of the salinity equation acts as to increase the salinity amplitude. That leads to a very attractive opportunity to close the circulation problem at the fourth order. At this level, the nonlinearity counteracts the background stratification term (49), calling for its inclusion in the fourth-order balance and, ultimately, results in a unique solution. And indeed, as shown above, consideration of the fourth-order balances makes it possible to form the amplitude equation (46) by sequentially eliminating the higher-order terms in favour of the lower-order components, eventually arriving at the explicit expression for W_0 .

Since the foregoing theory was developed for modon of unit radius, to reconstruct the general solution it only remains to rescale our variables using (27). The numerical simulations and theoretical considerations in §2 suggest that the scale of double-diffusive modons is set by the salinity dissipation scale λ_s , which is proportional to $\sqrt{\tau}$. Thus, we arrive at explicit predictions for the actual propagation velocity and the T – S amplitudes (denoted by a tilde) in double-diffusive modons:

$$\tilde{W} \propto \frac{W}{\tau^{2.5}}, \quad \tilde{T} \propto \frac{T_{tot}}{\tau^{1.5}}, \quad \tilde{S} \propto \frac{S_{tot}}{\tau^{1.5}}. \quad (50)$$

4. Large-scale implications

4.1. The modon flux model

In this section, we formulate the physically motivated laws for the vertical transport of heat and salt as a function of large-scale T – S gradients. Based on considerations in §2, we attribute the vertical salt flux to the exchange of fluid by double-diffusive modons,

whereas for heat, owing to its higher molecular diffusivity, mixing can also be driven by short-lived and less-coherent structures. Thus, the salt flux (F_S) is determined by the salt anomaly of the modons, their propagation velocity, and concentration:

$$F_S \propto \frac{A_{mod}}{A_{total}} \tilde{W} \langle \tilde{S} \rangle, \quad (51)$$

where angle brackets denote the spatial average over the modon area. Recalling that the fraction of area occupied by modons (A_{mod}/A_{total}) was assumed (see (14)) to be proportional to τ , we reduce (51) to

$$F_S \propto \tau \tilde{W} \langle \tilde{S} \rangle. \quad (52)$$

Combining (41), (42), (50), and (52), we write down the two leading terms of the asymptotic ε -expansion for the salt flux:

$$F_S \propto F_0 \varepsilon^{-1} + F_2 + \dots, \quad (53)$$

where

$$\left. \begin{aligned} F_0 &= \frac{W_0 \langle S_0 \rangle}{\tau^3}, \\ F_2 &= \frac{W_2 \langle S_0 \rangle + W_0 \langle S_{20} \rangle}{\tau^3}. \end{aligned} \right\} \quad (54)$$

Since (W_0 , W_2 , S_0 , S_{20}) are readily available from the foregoing asymptotic theory (§3), we arrive at the explicit prediction for the velocity of modons and their salt flux F_S :

$$|\tilde{W}| \approx k_1 (\varepsilon^{-3/4} + C_1 \varepsilon^{1/4}), \quad (55)$$

and (53), (54) similarly yield:

$$|F_S| \approx k_2 (-\varepsilon^{-1} + C_2), \quad (56)$$

where $k_1 \propto 1/\sqrt{\tau}$ and k_2 is an order-one constant. The constants C_1 and C_2 can be evaluated for each (τ, Pr) . Thus, for $(\tau, Pr) = (\frac{1}{3}, 7)$, our model predicts $C_1 = -0.94$ and $C_2 = -2.55$. For smaller values of the diffusivity ratio, we compute C_1 and C_2 by taking the $\tau \rightarrow 0$ limit in all equations leading to (55) and (56), in which case we arrive (for $Pr = 7$) at $C_1 = -0.72$ and $C_2 = -2.17$.

Next, we compare the theoretical predictions (55) and (56) with direct numerical simulations over a range of τ and R_ρ (in all cases $Pr = 7$). All the experiments were performed on the computational domain corresponding to 10×10 fastest growing finger wavelengths (d), which was resolved by a uniform mesh with $(N_x \times N_z) = (1024 \times 1024)$ elements. These numerical experiments are summarized in table 1 and the resulting equilibrium fluxes are consistent with earlier studies (e.g. Stern & Simeonov 2005). Thus, our modon flux model can be viewed as an attempt to explain these numerical results from first principles.

4.2. Dependence on the density ratio

In order to test the prediction (55) and (56), we turn to the subset of experiments in table 1 with $\tau = \frac{1}{3}$ ($R_\rho = 1.1, 1.2, 1.3, 1.4,$ and 1.5) and examine how the intensity of salt fingering varies with R_ρ . To test (55), we assume that the propagation velocity of modons is comparable to the average (RMS) vertical velocity. This assumption is reasonable for order-one values of the diffusivity ratio, in which case the modons occupy a substantial fraction of the total area of the computational domain (see the discussion in §2) and their propagation velocities may control the average vertical

		$\tau = \frac{1}{3}$	$\tau = \frac{1}{6}$	$\tau = \frac{1}{12}$	$\tau = \frac{1}{24}$	$\tau = \frac{1}{48}$
$R_\rho = 1.1$	$ F_S $	171.0		294.0		
	$ F_T $	147.0		231.0		
	γ	0.858		0.784		
$R_\rho = 1.2$	$ F_S $	89.4	141.0	160.0	180.0	197.0
	$ F_T $	75.3	111.0	118.0	128.0	137.0
	γ	0.842	0.787	0.739	0.711	0.695
$R_\rho = 1.3$	$ F_S $	56.6	87.7	113.0	123.0	141.0
	$ F_T $	47.4	67.3	81.6	84.2	94.8
	γ	0.837	0.767	0.723	0.685	0.673
$R_\rho = 1.4$	$ F_S $	37.0		79.5		
	$ F_T $	30.8		56.2		
	γ	0.833		0.707		
$R_\rho = 1.5$	$ F_S $	26.4		61.3		
	$ F_T $	21.9		42.8		
	γ	0.832		0.698		

TABLE 1. Summary of the numerical experiments. Each experiment was performed with the computational domain corresponding to 10×10 fastest growing finger wavelengths, resolved by $(N_x \times N_z) = (1024 \times 1024)$ elements, and the Prandtl number is $Pr = 7$. In each cell, the first number is the equilibrium non-dimensional salt flux, the second number is the non-dimensional heat flux (the Nusselt number), and the third number represents the flux ratio γ .

velocity w_{RMS} . Note that the situation could be very different for $\tau \ll 1$, when modons are relatively small and their motion may not contribute much to w_{RMS} . For each run, the vertical RMS velocity is plotted as a function of $1/\varepsilon$ in figure 7. The dependence of w_{RMS} on ε is consistent with (55): in figure 5 we also plot the best fit of the numerical data $w_{RMS}(\varepsilon)$ to the theoretical profile $k_1(\varepsilon^{-0.75} + C_1\varepsilon^{0.25})$ with k_1, C_1 as parameters. The fitted profile (solid curve) describes the raw data (plus signs) exceptionally well. The best fit approximates the numerical data as

$$w_{RMS} = 7.33(\varepsilon^{-0.75} - 1.22\varepsilon^{0.25}). \quad (57)$$

It is interesting to note that the asymptotic expression (55) predicts $C_1 = -0.94$ for $\tau = \frac{1}{3}$, which is not very different from the numerical value of $C_1 = -1.22$ in (57). This result indicates that the theoretical model offers a fair estimate even for the weak effects that are high order in ε .

Figure 8(a) presents the average non-dimensional salt flux (F_S) as a function of $1/\varepsilon$ for the foregoing (figure 7) numerical experiments. The numerical $F_S(\varepsilon)$ dependence conforms to the pattern (56) suggested by the formal asymptotic expansion. In figure 8(a) we also show the best fit of the numerical data $F_S(\varepsilon)$ to the theoretical profile $k_2(\varepsilon^{-1} + C_2)$ with k_2, C_2 as parameters. Apparently, the fitted profile (solid straight line) describes the raw data (denoted by plus signs) exceptionally well. The best fit approximates the numerical data as

$$|F_S| = 91.1(\varepsilon^{-1} - 1.46). \quad (58)$$

The difference between $C_2 = -2.55$ predicted by the asymptotic expression in (56) for $\tau = \frac{1}{3}$ and the numerical value of $C_2 = -1.46$ in (58) can be readily attributed to the numerous idealizations of the theoretical model. These include the perfectly circular shape of modons, their rectilinear pattern of motion, disregard of modon-modon

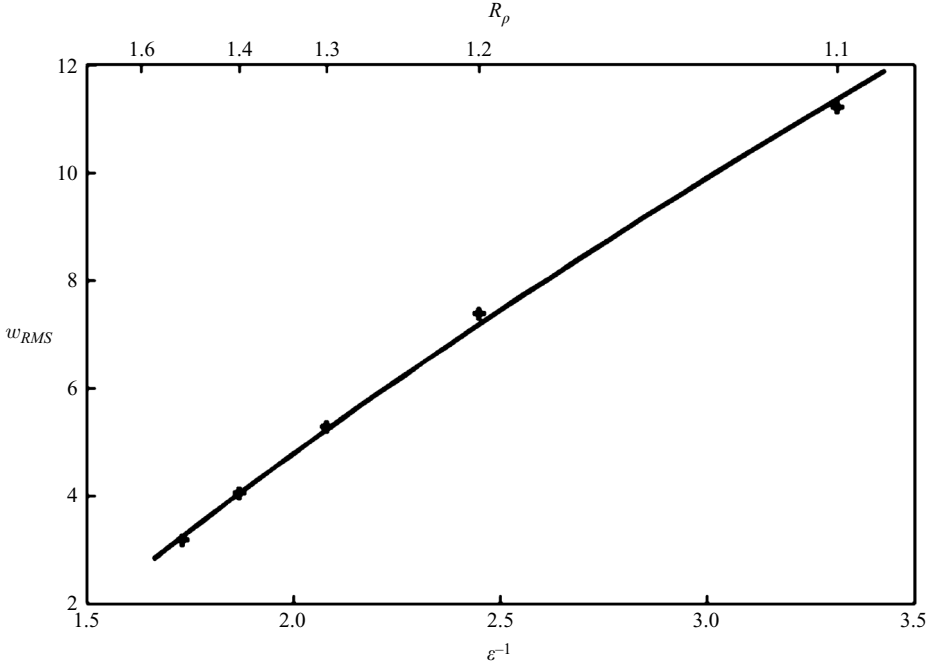


FIGURE 7. The vertical (RMS) velocity, averaged in space and time, as a function of $1/\varepsilon = 1/\sqrt{1 - R_\rho^{-1}}$ for $(\tau, Pr) = (\frac{1}{3}, 7)$. The numerical data, denoted by plus signs, follow the theoretical pattern (solid curve) predicted for the speed of double-diffusive modons.

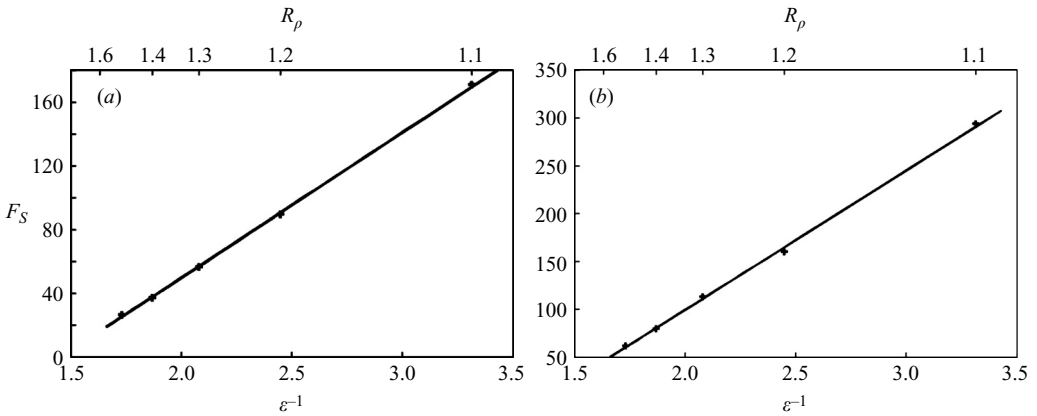


FIGURE 8. Comparison of the theoretical expression for the non-dimensional salt flux (F_S) as a function of $1/\varepsilon = 1/\sqrt{1 - R_\rho^{-1}}$ with the results of numerical experiments for (a) $\tau = \frac{1}{3}$ and (b) $\tau = \frac{1}{12}$. The two leading-order terms in the asymptotic $\varepsilon \rightarrow 0$ expansion correspond to the linear relation (56) between F_S and ε^{-1} , and the distribution of the numerical data (plus signs) is well represented by straight lines, both in (a) and (b).

collision effects, and the asymptotically small ε . Fitting the three-term (rather than two-term) series to the numerical data also improves the data/theory agreement by raising the coefficient C_2 to -1.78 .

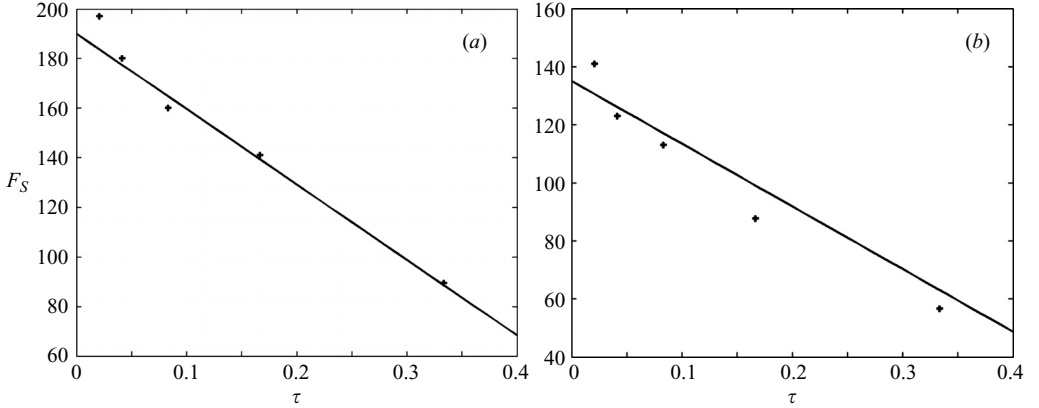


FIGURE 9. Comparison of the theoretical expression for the non-dimensional salt flux (F_S) as a function of τ with the results of numerical experiments for (a) $R_\rho = 1.2$ and (b) $R_\rho = 1.3$. The two leading-order terms in the asymptotic $\tau \rightarrow 0$ expansion for F_S correspond to the linear relation (60) between F_S and τ . The distribution of the numerical data (plus signs) is well represented by straight lines with the coefficient of -1.6 in the τ -term (see (60)), both in (a) and (b).

It is of interest to test our theoretical predictions for different values of the diffusivity ratio. Therefore we turn to the experiments in table 1 with $\tau = \frac{1}{12}$. The numerical values of F_S are plotted as a function of ε^{-1} in figure 8(b). Although the magnitude of fluxes increases considerably relative to that in figure 8(a), their dependence on the density ratio is still accurately captured by the expression (56). The best fit of the numerical data (plus signs) by the theoretical profile $k_2(\varepsilon^{-1} + C_2)$ is indicated by the straight line, which approximates fluxes as

$$|F_S| = 146(\varepsilon^{-1} - 1.32). \quad (59)$$

4.3. Dependence on the diffusivity ratio

The theoretical model predicts the convergence of the salt flux to a finite value in the limit $\tau \rightarrow 0$. To be more explicit in describing the flux pattern for small finite diffusivity ratios, we focus on the leading-order term of our ε -expansion in (53): $F_S \propto F_0 \varepsilon^{-1}$. Using (10), (28), (47), (48), and (54), we evaluate the two leading terms of the Taylor expansion of F_0 in τ , which (for $Pr = 7$) yields

$$|F_S| \approx K(1 - 1.6\tau) + O(\tau^2), \quad (60)$$

where $K(\varepsilon)$ is the salt flux at $\tau \rightarrow 0$. Equation (60), for instance, implies that the decrease of diffusivity ratio from $\tau = \frac{1}{3}$ towards zero should be accompanied by an almost twofold increase in flux. To test the prediction in (60) we performed a series of experiments with diffusivity ratios of $\tau = \frac{1}{3}, \frac{1}{6}, \frac{1}{12}, \frac{1}{24}, \frac{1}{48}$ and $(R_\rho, Pr) = (1.2, 7)$. The numerical salt fluxes are plotted as a function of τ in figure 9(a). Apparently, the $F_S(\tau)$ pattern is adequately captured by the asymptotic relation (60). Numerical points (plus signs in figure 9a) are distributed along the line with slope consistent with the coefficient -1.6 in (60). The theoretical relation $F_S = K(1 - 1.6\tau)$ with $K = 190$ is also shown in figure 9(a). In figure 9(b), the same diagnostics are applied to a set of experiments with $R_\rho = 1.3$. We plot the numerical values for $F_S(\tau)$, denoted by plus signs, along with the asymptotic ($\tau \ll 1$) relation $F_S = K(1 - 1.6\tau)$ with $K = 135$ (solid line). Their apparent agreement once again supports the proposed modon flux laws.

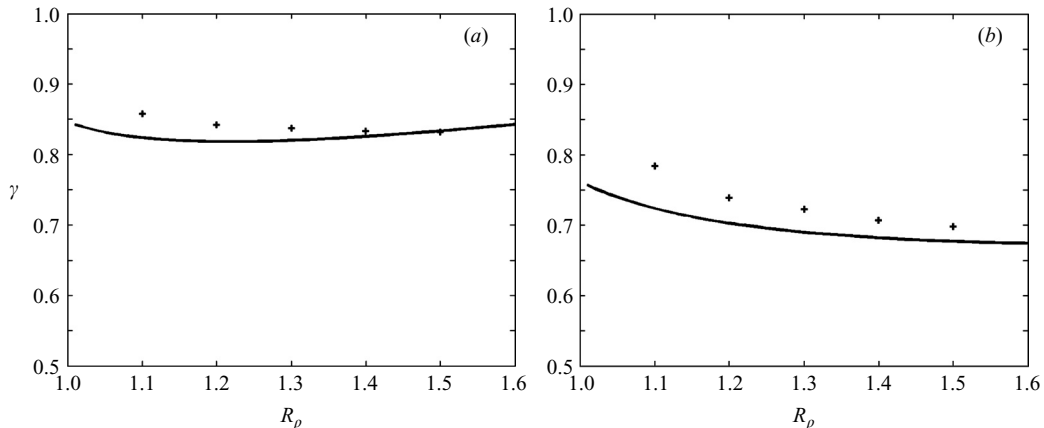


FIGURE 10. Flux ratio γ as function of density ratio for (a) $\tau = \frac{1}{3}$ and (b) $\tau = \frac{1}{12}$. Plus signs denote the numerical experiments summarized in table 1 and the solid curves represent Schmitt's (1979) fastest growing finger model.

Finally, we note that from the foregoing salt flux model it is straightforward to calculate the heat flux and the kinetic energy dissipation rate:

$$F_T = \gamma F_S, \quad D_v = (1 - \gamma) F_S, \quad (61)$$

where γ is the flux ratio. The flux ratio is a fairly stable characteristic of salt-finger convection; its typical values and dependences are adequately explained by the linear stability considerations. In figure 10, we plot our numerical data for $\gamma(R_\rho)$, denoted by plus signs, along with the flux ratio of the linearly fastest growing finger model (Schmitt 1979). While numerical values are slightly offset from the theoretical curve towards larger γ , these results indicate that Schmitt's model remains surprisingly accurate in predicting the flux ratio even in the strongly nonlinear low- R_ρ regime. As discussed earlier (§2), the transport characteristics of double-diffusive modons place the nonlinear constraint on the flux of the slower diffuser (S), whereas the rate of the T -flux is set by the balances operating on the forcing scale – the linearly fastest growing finger width.

5. Conclusions

Traditionally, most theoretical models of salt fingers (e.g. Schmitt 1979; Radko & Stern 2000; Stern & Simeonov 2005) sought the solutions representing long vertically oriented finger-like structures. While tall narrow salt fingers can be realized at high density ratios (R_ρ), the laboratory, field, and numerical experiments indicate that tall structures cannot survive when the density ratio is sufficiently low. For instance, Taylor (1993) investigated the anisotropy of salt fingers in the laboratory and suggested that the fully developed salt fingers could be considered roughly isotropic for $R_\rho < 5$, noting that the finger aspect ratio tends to approach unity for $R_\rho \rightarrow 1$. These results are consistent with the *in situ* oceanic measurements of salt fingers by a horizontally towed device (Lueck 1987). Lueck found very little coherence between the temperature records of two sensors vertically separated by 6 cm – a distance comparable to the dominant scale of primary salt-finger instability at that location. This lack of vertical coherence casts doubt on the relevance of models which picture salt fingers as tall and vertically oriented.

The two-dimensional numerical simulations reveal that at low density ratios, tall fingers are replaced by coherent dipolar eddies – the double-diffusive modons – which move vertically while roughly preserving their structure and temperature/salinity anomalies. In this paper we argue that the exchange of fluid by double-diffusive modons controls the vertical mixing of heat and salt. The flow pattern in double-diffusive modons and their terminal velocities are explained using an asymptotic expansion in which the parameter $\varepsilon = \sqrt{1 - R_\rho^{-1}}$ is small. This analytical solution is the basis of a phenomenological mixing model in which salt finger convection is represented by an array of vertically translating double-diffusive modons. The theory predicts that, at the leading order, the eddy heat/salt fluxes are linearly related to ε^{-1} :

$$(F_T, F_S) \propto \frac{1}{\sqrt{1 - R_\rho^{-1}}}, \quad (62)$$

and that the proportionality coefficients are only weakly dependent on the diffusivity ratio ($\tau = k_S/k_T$), as long as $\tau \ll 1$. The proposed mixing model is successfully tested by direct numerical simulations.

While this paper is focused on the salt-finger case, we expect to find, and describe analytically, double-diffusive modons in fully developed diffusive convection, cold fresh fluid above warm and salty. In diffusive convection, the search might be focused on the vertically oscillating (rather than the rectilinearly propagating) structures. We are equally optimistic with regard to the prospects of extending our theory and modelling to three dimensions, where we anticipate the appearance of axisymmetric translating rings – three-dimensional counterparts of the double-diffusive modons. Although the coefficients of the resulting flux–gradient laws may vary considerably with the particular double-diffusive regime and the number of spatial dimensions, we speculate that the scaling laws formulated herein are of broader relevance.

The author thanks William Merryfield, Ray Schmitt, Melvin Stern, and reviewers for helpful comments. Support of the National Science Foundation (grant OCE 0547650) is gratefully acknowledged.

REFERENCES

- BALMFORTH, N. J., GHADGE, S. A., KETTAPUN, A. & MANDRE, S. D. 2006 Bounds on double-diffusive convection. *J. Fluid Mech.* **569**, 29–50.
- BATCHELOR, G. K. 1959 Small-scale variation of convected quantities like temperature in turbulent fluid. Part I. General discussion and the case of small conductivity. *J. Fluid Mech.* **5**, 113–133.
- BATCHELOR, G. K. 1969 Computation of the energy spectrum in homogeneous two-dimensional turbulence. *Phys. Fluids (Suppl. 2)* **12**, 233–238.
- KUNZE, E. 2003 A review of salt fingering theory. *Prog. Oceanogr.* **56**, 399–417.
- LAMB, H. 1895 *Hydrodynamics*. Cambridge University Press.
- LARICHEV, V. D. & REZNIK, G. M. 1976 Two-dimensional Rossby soliton: An exact solution. *Rep. USSR Acad. Sci.* **231**, 1077–1079.
- LUECK, R. G. 1987 Microstructure measurements in a thermohaline staircase. *Deep-Sea Res.* **34**, 1677–1688.
- MALKUS, W. V. R. & VERONIS, G. 1958 Finite amplitude cellular convection. *J. Fluid Mech.* **4**, 225–260.
- MERRYFIELD, W. J. & GRINDER, M. 1999 Salt fingering fluxes from numerical simulations (unpublished manuscript).
- MONIN, A. S. & OZMIDOV, R. V. 1985 *Turbulence in the Ocean*. D. Reidel.

- RADKO, T. 2003 A mechanism for layer formation in a double-diffusive fluid. *J. Fluid Mech.* **497**, 365–380.
- RADKO, T. 2005 What determines the thickness of layers in a thermohaline staircase? *J. Fluid Mech.* **523**, 79–98.
- RADKO, T. & STERN, M. E. 1999 Salt fingers in three dimensions. *J. Mar. Res.* **57**, 471–502.
- RADKO, T. & STERN, M. E. 2000 Finite amplitude salt fingers in a vertically bounded layer. *J. Fluid Mech.* **425**, 133–160.
- SCHLICHTING, H. & GERSTEN, K. 2000 *Boundary Layer Theory*. Springer.
- SCHMITT, R. W. 1979 The growth rate of supercritical salt fingers. *Deep-Sea Res.* **26A**, 23–44.
- SCHMITT, R. W. 1994 Double diffusion in oceanography. *Annu. Rev. Fluid Mech.* **26**, 255–285.
- SCHMITT, R. W. 2003 Observational and laboratory insights into salt finger convection. *Prog. Oceanogr.* **56**, 419–433.
- SHEN, C. Y. & VERONIS, G. 1997 Numerical simulation of two-dimensional salt fingers. *J. Geophys. Res.* **102**, 23131–23143.
- STERN, M. E. 1960 The “salt-fountain” and thermohaline convection. *Tellus* **12**, 172–175.
- STERN, M. E. 1975a Minimal properties of planetary eddies. *J. Mar. Res.* **33**, 1–13.
- STERN, M. E. 1975b *Ocean Circulation Physics*. Academic.
- STERN, M. E. & RADKO, T. 1998 The salt finger amplitude in unbounded T-S gradient layers. *J. Mar. Res.* **56**, 157–196.
- STERN, M. E., RADKO, T. & SIMEONOV, J. 2001 3D salt fingers in an unbounded thermocline with application to the Central Ocean. *J. Mar. Res.* **59**, 355–390.
- STERN, M. E. & SIMEONOV, J. 2005 The secondary instability of salt fingers. *J. Fluid Mech.* **533**, 361–380.
- TAYLOR, J. 1993 Anisotropy of salt fingers. *J. Phys. Oceanogr.* **23**, 554–565.